Ionics (2021) 27:4793–4800
https://doi.org/10.1007/s11581-021-04255-y

ORIGINAL PAPER

Hydrothermal reaction induced phase transition of vanadium oxide towards high-performance zinc ion batteries cathode

Chen-Yang Tian[1,2] · You-De Li[3] · Dan-Ni Du[1,2] · Yu-Shan Zhang[1,2] · Bing-Mei Zhang[1,2] · Dong-Ting Zhang[1,2] · Ling-Bin Kong[1,2] · Mao-Cheng Liu[1,2]

Received: 12 July 2021 / Revised: 27 August 2021 / Accepted: 29 August 2021 / Published online: 9 September 2021

Abstract

Aqueous zinc ion batteries (ZIBs) are widely researched due to the low-cost and intrinsic safety. However, the rate capability and specific capacity of ZIBs is limited due to the dissolution and structural collapse of cathode materials. It is crucial to construct stable cathode materials to promote rate capability and cycle stability of ZIBs. In this paper, The V_3O_7 was tightly attached to the surface of graphene oxide (GO) by a hydrothermal reaction and a V_3O_7/GO heterostructure was successfully achieved. The GO could increase structural stability, enhance electrical conductivity, and expand specific surface area of V_3O_7. Therefore, the V_3O_7/GO with a heterostructure exhibits an improved cycle stability and rate capability compared with V_3O_7. It displayed a specific capacity of 275.6 mA h g^{-1} at a current density of 1.0 A g^{-1}. The study paves the way for promoting the Zn^{2+} storage performance of vanadium oxide and developing stable cathode materials of ZIBs.

Keywords Zinc ion batteries · Heterostructure · Vanadium oxide · Zinc ions storage

Introduction

Aqueous zinc ion batteries (ZIBs) are becoming an ideal candidate in new energy storage equipment areas due to the excellent safety, non-toxic electrolyte, and environment friendly [1–3]. However, the development of ZIBs has been hindered because of lack of suitable cathode materials that extend cycle life and high-rate capability [4–6]. Despite manganese-based oxides [7, 8], Quinone analogs [9] and Prussian blue analogs [10], as well as sustainable Chevrel phase compounds [11, 12], have been widely researched in the field of ZIBs. The development of stable cathode materials remains a huge challenge due to the low specific capacity and poor cycle stability.

Among the reported cathode materials, vanadium-based oxide possesses outstanding framework structures that have been widely studied due to various redox reactions and the layered structure provides space for the insertion of Zn^{2+} [13–20]. However, most of them are still plagued by the dissolution of vanadium oxide and the formed of electrochemically byproduct during cycling, leading to capacity fading and limited cycle stability. Several methods have been mentioned to increase the capacity and improve cycle stability of vanadium oxide. Wang et al. [21] confirmed that barium ions inserted into the interlayer of vanadium oxide can promote the electrochemical performance of $Ba_{1.2}V_6O_{16}{\cdot}3H_2O$ by enhancing the stability of vanadium oxide and accelerating the diffusion rate of Zn^{2+}. Liang et al. [22] presented the mixed vanadium valence states (V^{4+}/V^{5+}) of V_6O_{13} with open framework structure, which exhibits an excellent rate capability and outstanding specific capacity of 206 mA h g^{-1} at a current density of 10 A g^{-1}. Tamilselvan et al. [23] reported that the $(NH_4)_{0.37}V_2O_5.0.15(H_2O)$ possesses highly crystalline, which displays the initial specific capacity of 400 mA h g^{-1} at the current density of 0.5 A g^{-1}. Besides, V_2O_5 with pre-embedded water molecules and/or metal/nonmetal ions [24, 25], vanadate complex [26, 27], and other vanadium oxide with layered/tunneled structures [28–31] can also be employed as cathode materials of ZIBs. These reports have demonstrated the excellent Zn^{2+} storage performance by employing the pre-embedded metal/nonmetal

✉ Mao-Cheng Liu
liumc@lut.edu.cn

[1] State Key Laboratory of Advanced Processing and Recycling of Non-Ferrous Metals, Lanzhou University of Technology, Lanzhou 730050, China

[2] School of Materials Science and Engineering, Lanzhou University of Technology, Lanzhou 730050, China

[3] Chaowei Power Group Co., LTD, Changxing 313100, China

ions or change the structure of vanadium oxide. However, volume expansion of vanadium oxide during Zn^{2+} insertion/extraction and low conductivity continues to impede the development of ZIBs. How to effectively alleviate the volume expansion and improve the conductivity possesses important significance to the performance improvement of the cathode materials.

In this study, the GO-supported V_3O_7/GO heterostructures with mixed valence states are prepared by a hydrothermal method. The mixed valence states can provide more possibilities for redox reaction, which is beneficial to the reaction. The V_3O_7 nanosheets were attached on the surface of GO, which increase specific surface area of V_3O_7/GO heterostructures. The stability was improved due to the hydrogen bonds between V_3O_7 and the functional groups on the surface of GO, which increases the specific capacity, cycle stability, and rate capability. The V_3O_7/GO heterostructures show an outstanding cycle stability, rate capability, and impart fast ion storage kinetics to electrode material due to rapid ion/electron diffusion and stable structure. The Zn//V_3O_7/GO heterostructures battery possesses an excellent practicability and high safety in application devices. The results can provide a guidance for the design of high cycle stability zinc ion batteries.

Experimental section

Preparation of sample

A total of 20 mL 1.5 mM citric acid solution was slowly added into 30 mL 2 mM NH_4VO_3 solution at 65 °C and stirring for 2 h. Twenty milliliters of graphene oxide dispersion (1 mg/mL) was added to the solution and stirring for 3 h. Then the obtained solution was poured autoclave lined and heated at 200 °C for 24 h to conduct a hydrothermal reaction. Finally, V_3O_7/GO heterostructures were obtained after washing the product with deionized water and acetone five times and dried in oven at 65 °C for 10 h. For comparison, V_2O_5 nanosheets were synthesized without adding GO.

Characterization

The phase of the samples is analyzed using a D/max-2110 PC X-ray diffraction (XRD, Japan). The elemental composition was confirmed through X-ray photoelectron spectroscopy (XPS, PHI 5700). The microstructures were examined employing a JSM-IT100 field-emission scanning electron microscope (SEM; JEOL, Japan) and a JEM-2100 Plus transmission electron microscope (TEM; JEOL, Japan). The Brunauere-Emmette-Teller (BET) surface area was tested employing the specific surface area analyzer (JW-BK200, JWGB SCI. & TECH).

Electrochemical measurements

The electrochemical performance of V_3O_7/GO heterostructures was research as cathode, zinc foil as anode with 3 M $ZnSO_4$ as electrolyte by assembled CR-2032 type coin batteries. The cathodes on stainless steel foil were synthesized by smearing slurry, containing 70 wt% of active material, 10 wt% of polyvinylidene fluoride (PVDF), and 20 wt% acetylene black together with the appropriate quantity of N-methyl pyrrolidinone (NMP) dried at 60 °C for 12 h. Then the electrode was placed in a vacuum oven and heated at 80 °C for 12 h. Finally, the electrodes were cut into a disk with 7 mm radius after 5 min at 12 MPa. The mass loading amount of active material for V3O7/GO heterostructures electrodes in the electrochemical characterization is 0.7 mg cm^{-2}. The galvanostatic charge/discharge (GCD) was tested by the land battery testing system with 0.2–1.6 V voltage. The cyclic voltammetry (CV) and electrochemical impedance spectroscopy (EIS) were studied by the CHI660E electrochemical workstation.

Results and discussion

The preparation procedures of V_3O_7/GO heterostructures are showed in Fig. 1a, and the uniform V_3O_7/GO heterostructures were produced with hydrothermal reaction. The X-ray diffraction (XRD) pattern of V_3O_7/GO heterostructures is shown in Fig. 1b, and the peaks located at 24.9° and 49.5° correspond to the (− 111) and (020) plane of V_3O_7 (JCPDS No.27–0940), while the sharp peak at 8.5° indicates the (001) plane of GO. Differently, vanadium oxide without adding GO corresponds to the standard card of V_2O_5 (JCPDS No.72–0433) in Figure S1. The TG curve of V_3O_7/GO heterostructures is displayed in Figure S2. Through calculation, the content of GO is 9.3271%. There is no obvious water content missing, which proves that the cathode material is V_3O_7/GO. The valence of vanadium was changed due to the enhanced reducibility of citrate acid after the addition of GO, which resulted in conversion of V^{5+} to V^{4+}. The valence state and element composition were researched by the X-ray photoelectron spectroscopy (XPS) measurement and the XPS survey spectrum of V_3O_7/GO heterostructures displays characteristic peaks of C 1 s, O 1 s, and V 2p, which explains that the V_3O_7/GO heterostructures are composed of C, O, and V elements (Fig. 1c), comparing with the V_2O_5 only exists V and O elements (Figure S3a). The high-resolution XPS spectra of V 2p for V_3O_7/GO heterostructures are demonstrated in Fig. 1f, where the peaks of V $2p_{3/2}$ and V $2p_{1/2}$ correspond to 517.2 and 524.4 eV, respectively [32]. The V $2p_{3/2}$ peak

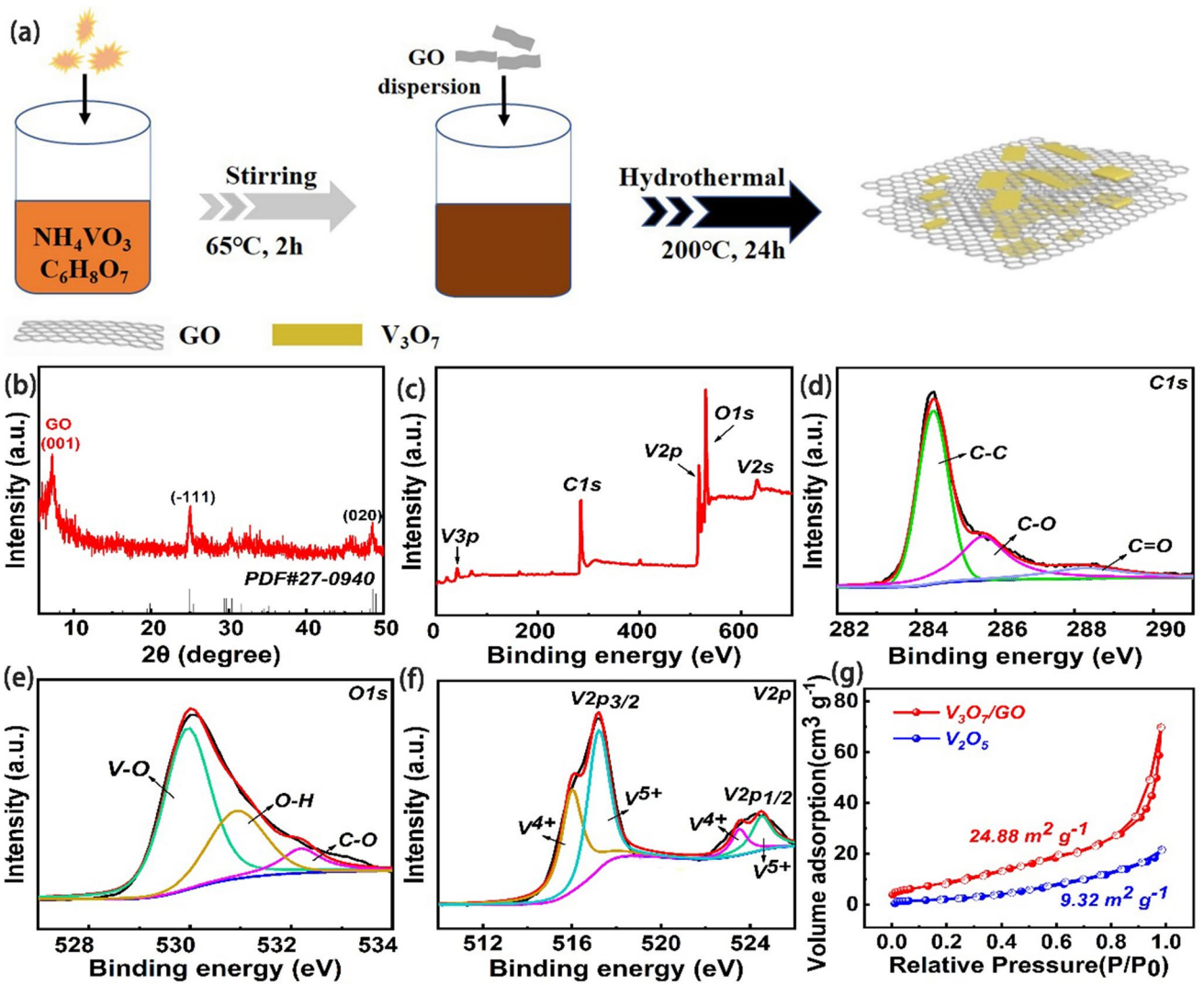

Fig. 1 **a** Schematic diagram of preparation procedures of V_3O_7/GO heterostructures, **b** XRD patterns, **c** XPS survey spectrum, **d** C 1 s, **e** O 1 s, **f** V 2p core-level spectra of V_3O_7/GO heterostructures, **g** nitrogen adsorption/desorption curves of V_3O_7/GO heterostructures and V_2O_5

is divided into two peaks at binding energies of 515.9 and 517.2 eV, which corresponded to V^{4+} and V^{5+}, respectively [33]. Compared with V_2O_5 (Figure S3c), the appearance of V^{4+} in V_3O_7/GO heterostructures is due to the reduction of V^{5+} to V^{4+} when the GO is present. The C 1 s core levels of V_3O_7/GO heterostructures are exhibited in Fig. 1d. The peaks at 288.4, 285.8, and 284.3 eV are attributed to the C = O, C–O, and C–C bonds of GO, respectively [34]. The O 1 s core levels of V_3O_7/GO heterostructures (Fig. 1e) exhibit three peaks at 529.8, 531.0, and 532.5 eV, respectively, the peak of V–O bonds is assigned at 529.8 eV, the peak at 531.0 eV is assigned to the attached residual water at the surface, and while the peak at 532.5 eV corresponds to –OH/–COOH groups of GO. The hydrogen bond between V_3O_7 nanosheets and –OH/–COOH groups on the surface of GO can buffer the expansion and contraction of V_3O_7/GO during the Zn^{2+} insertion/extraction process. Therefore, the O 1 s core levels of V_2O_5 are inconsistent with V_3O_7/GO heterostructures (Figure S3b). The specific surface areas of V_3O_7/GO heterostructures and V_2O_5 (Fig. 1g) are obtained by nitrogen adsorption/desorption measurement as 24.88 $m^2\ g^{-1}$ and 9.32 $m^2\ g^{-1}$. The results proved that the importing of GO can increase the specific surface area of V_3O_7, which provides more active sites and is promising to obtain a high capacity. Moreover, the GO can also serve as electron-conductive frameworks that could improve the conductivity and structural stability of V_3O_7.

The scanning electron microscope (SEM) and transmission electron microscopy (TEM) images of V_3O_7/GO are exhibited in Fig. 2. The images of SEM present a heterostructures between V_3O_7 nanosheets and GO

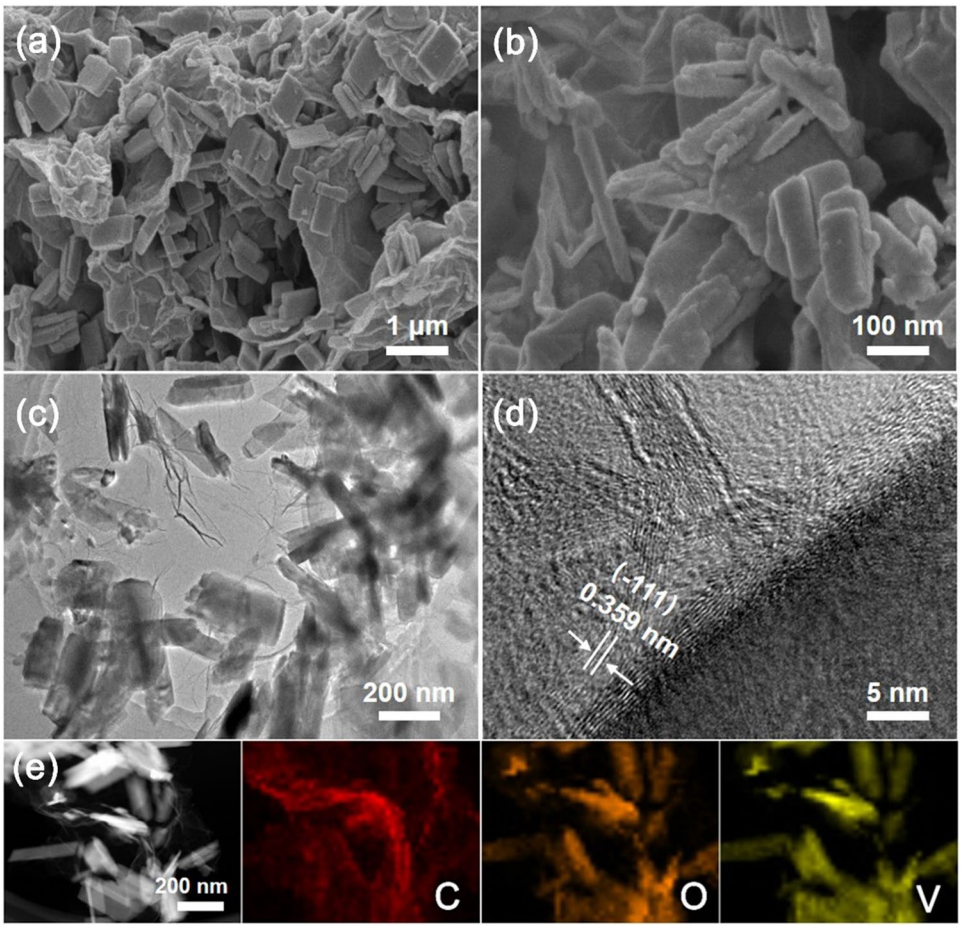

Fig. 2 **a** and **b** SEM images of the V_3O_7/GO heterostructures, **c** TEM image and **d** HRTEM image of V_3O_7/GO heterostructures, **e** TEM elemental mappings of C, O, and V elements in V_3O_7/GO heterostructures

layers (Fig. 2a–b), which is composed of interlaced V_3O_7 nanosheets. The heterostructures are further confirmed by TEM image (Fig. 2c), and V_3O_7 nanosheets were tightly attached on the surface of GO to form an ultrathin flat heterostructures which provide rapid diffusion channels for Zn^{2+}. By contrast, V_2O_5 is shown as a blocky structure in Figure S4, and the long pathway of Zn^{2+} ion diffusion in blocky structure is unsuitable to achieve a high-rate capability. The high-resolution transmission electron microscope (HRTEM) image of V_3O_7/GO heterostructures is shown in Fig. 2d, the interlayer spacing of 0.359 nm corresponding to the (− 111) planes of V_3O_7. The element distributions of V_3O_7/GO heterostructures are displayed in the TEM mapping (Fig. 2e), and the V, O, and C elements are uniformly distributed, which confirms that the V_3O_7 nanosheets were uniformly distributed on the surface of GO in the heterostructures. It can be explained that V_3O_7 nanosheets are connected with GO by hydrogen bonds between V–O and functional groups on the surface of GO. The GO can prevent the volume expansion of V_3O_7 and improve the conductivity of V_3O_7 due to its high mechanical strength and inherent conductivity, improving the cycle stability and rate capability.

The zinc storage performance of V_3O_7/GO heterostructures was evaluated employing Zn foil as anode and 3 M $ZnSO_4$ (saturated vanadium oxide) as electrolyte. The cyclic voltammetry (CV) curves at a scan rate of 0.1 mV s^{-1} are displayed in Fig. 3a. The second and third cycles are mildly different from the first cycle, which is attributed to activated process of electrode in the first cycle. The redox peaks at 0.74/0.60 V and 1.03/0.92 V can be found in the second cycle, which explains a mechanism of multistep zinc insertion/extraction reaction during the discharge/charge process. Compare with V_3O_7/GO, the CV curves of V_2O_5 exhibit an inferior consistency (Figure S5a), which confirms that an irreversible phase change occurred in the cyclic processes. The CV curves of V_3O_7 are exhibited in Figure S6a, which shows a similar shape to V_3O_7/GO heterostructures. The galvanostatic charge/discharge (GCD) curves of first three cycles of V_3O_7/GO heterostructures at a current density of 1.0 A g^{-1} are presented in Fig. 3b. The discharge capacity of first cycle is 275.6 mA h g^{-1} and the first three charge/discharge curves are almost overlapped, suggesting the outstanding cycle stability of V_3O_7/GO heterostructures. The GCD curves of V_2O_5 are shown in Figure S5b, which has the same voltage plateaus compare to V_3O_7/GO

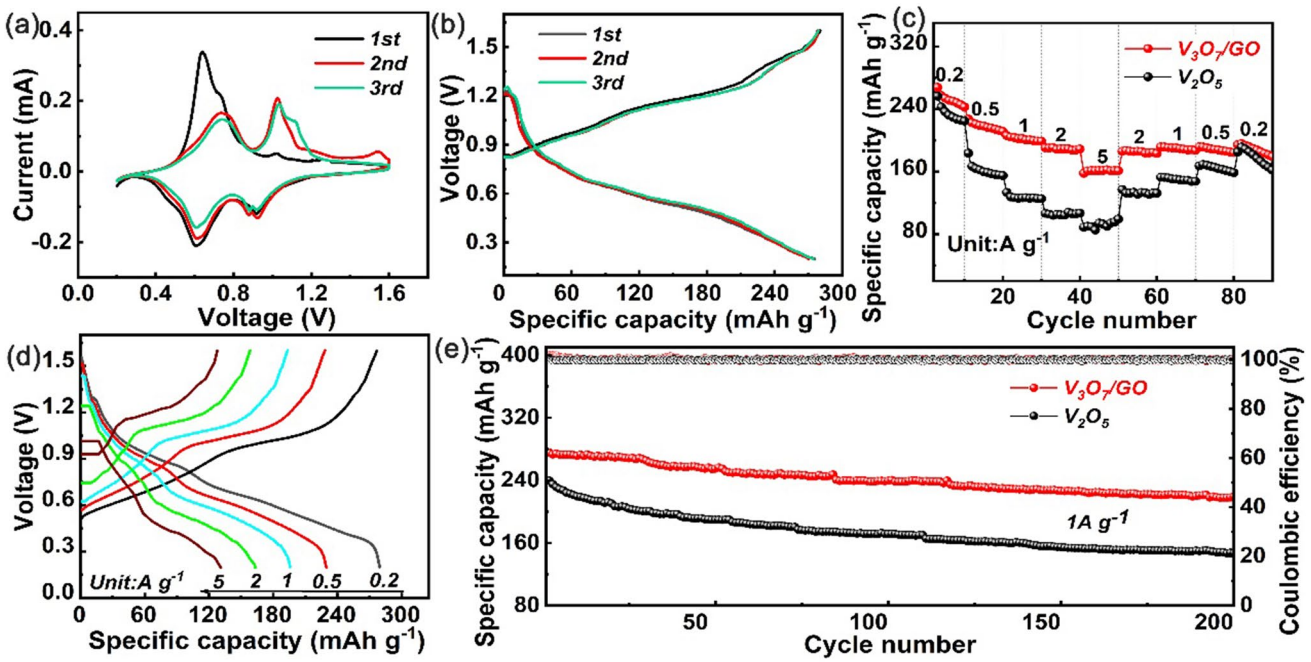

Fig. 3 **a** The cyclic voltammetry curves of the first three cycles at 0.1 mV s^{-1}, **b** galvanostatic charge/discharge curves at 0.1 A g^{-1}, **c** rate capability at the different current densities, **d** galvanostatic charge/discharge curves at the different current densities, **e** the cycle stability at a current density of 1.0 A g^{-1}

heterostructures. The rate capability of V_3O_7/GO heterostructures at the different current densities is displayed in Fig. 3c and d, and the specific capacities are 268.0, 227.3, 206.1, 190.6, and 161.5 mA h g^{-1} at the current densities of 0.2, 0.5, 1.0, 2.0, and 5.0 A g^{-1}, respectively. The current density is 5 A g^{-1}, the specific capacity is 161.5 mA h g^{-1}, and the capacity retention rate is 60.3%. The specific capacity is restored to 195.9 mA h g^{-1} and the restoration ratio is 73.1% when the current density is recovered to 0.2 A g^{-1}. In comparison, the specific capacities of V_2O_5 are 236.5, 159.7, 126.5, 104.7, and 89.0 mA h g^{-1} at the same current densities (Figure S5c). The specific capacities of V_3O_7 are 185.8, 145.0, 125.0, 108.4, and 85.5 mA h g^{-1} at the same current densities (Figure S6b). The specific capacity is restored to 131.3 mA h g^{-1} and the restoration ratio is 68.3% when the current density is recovered to 0.2 A g^{-1}. The specific capacity and capacity retention of V_3O_7/GO heterostructures are superior to that of V_2O_5, which explains V_3O_7/GO heterostructures possess outstanding rate capability (Fig. 3c). The cycle stability of V_3O_7/GO heterostructures and V_2O_5 at the current density of 1.0 A g^{-1} is displayed in Fig. 3e, and a remarkable discharge capacity of 275.6 mA h g^{-1} is obtained for V_3O_7/GO heterostructures. The cycle stability of V_3O_7 at the current density of 1.0 A g^{-1} is displayed in Figure S6a, the specific capacity reaches 217.7 mA h g^{-1}, and the capacity retention is only 44.5% after 200 cycles. The long cycle performance of V_3O_7/GO heterostructures at the current density of 2.0 A g^{-1} is displayed in Figure S7, the specific capacity reaches 279.9 mA h g^{-1}, and remarkable capacity retention of about 76% after 200 cycles. It is obvious that the specific capacity of V_3O_7/GO heterostructures is higher than V_2O_5, which confirms that V_3O_7/GO heterostructures possess more active sites to storage Zn^{2+}. The cycle stability, rate capability, and specific capacity of V_3O_7/GO heterostructures are superior than V_2O_5 due to GO can improve conductivity, buffer expansion of volume, and increase specific surface area.

To further explore the storage kinetics behavior of Zn^{2+}, the CV curves were investigated that the scan rates from 0.2 to 1 mV s^{-1} as shown in Fig. 4a. The CV curves maintained the same shapes with the increased of scan rates from 0.2 to 1 mV s^{-1}, which demonstrats the outstanding rate capability and reversibility of reaction reversibility of V_3O_7/GO heterostructures. Compared with V_2O_5 (Figure S8a), the CV curves of V_3O_7/GO heterostructures show sharper redox peak, which suggests the faster reaction kinetics. To determine the capacity behaviors of Zn^{2+} storage in V_3O_7/GO heterostructures, the relationship between the peak current (i) and the scan rate (ν) of CV curves be expressed by the following formula [35]:

$$i = \alpha \nu^b$$
$$logi = blog\nu + log\alpha$$

where ν is the scan rate, i is the current response, and α and b are adjustable constants. The slope of log(i) versus

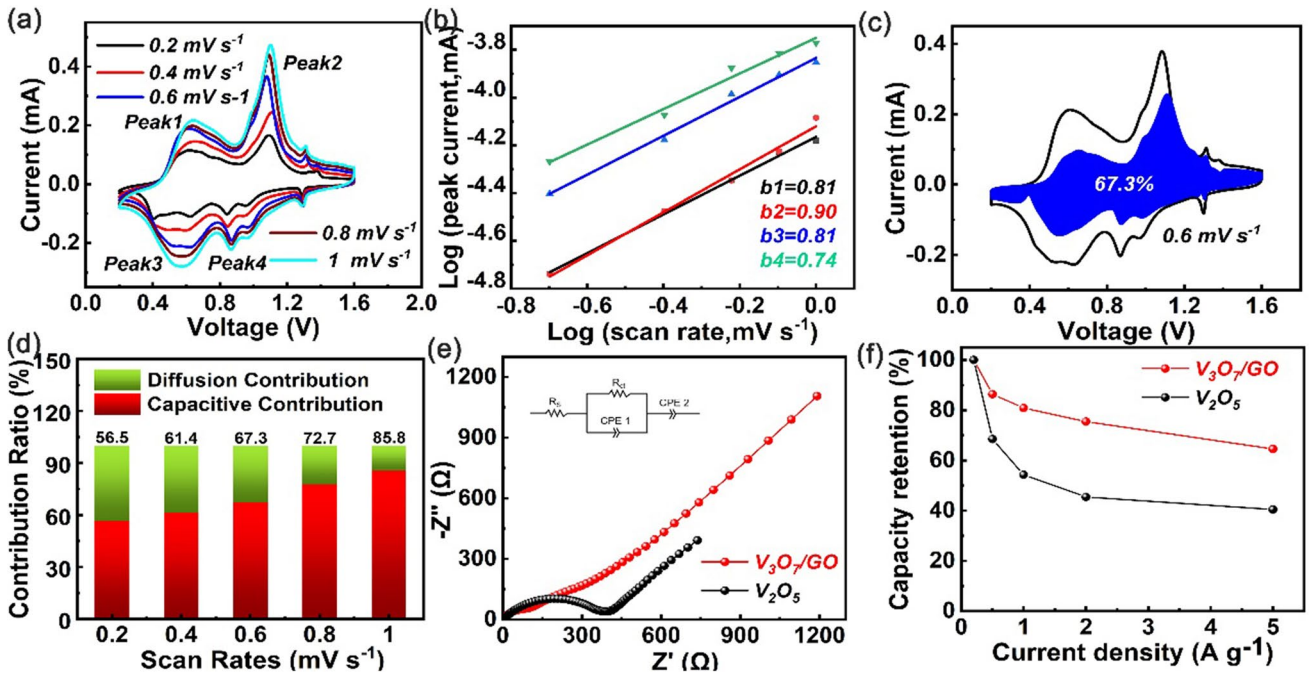

Fig. 4 **a** Cyclic voltammetry curves at different scan rates, **b** log(*i*)–log(*ν*) plots for specific peak currents. **c** Surface-controlled capacity contribution at 0.6 mV s^{-1}, **d** surface- and diffusion-controlled capacity contributions at different scan rates of V_3O_7/GO heterostructures, **e** Nyquist plots and **f** capacity retention of V_3O_7/GO heterostructures and V_2O_5 at different current densities

log(*ν*) plot is decided by the *b* value, which ranges from 0.5 to 1. The charging/discharging process is dominated by ion diffusion when $b = 0.5$, and $b = 1.0$ for a surface-controlled capacity dominates [36]. The *b* values of peaks 1, 2, 3, and 4 of V_3O_7/GO heterostructures are 0.81, 0.90, 0.81, and 0.74, respectively (Fig. 5b), while that of V_2O_5 are 0.82, 0.88, 0.76, and 0.70, respectively (Figure S8b), proving the mainly contributed by the surface-controlled process and the slight contributed by diffusion-controlled process in storage processes of Zn^{2+}. The surface-controlled process is crucial to achieve a high-rate capability compared with diffusion-controlled process. The capacitance contribution at a certain scan rate can be determined by employing the equation by [37]:

$$i = k_1 \nu + k_2 \nu^{1/2}$$

where k_1 and k_2 are constants, and the surface- and diffusion-controlled capacity contributions can be determined by considering the ratio of k_1 and k_2. To clarify this case, the surface-controlled capacity contribution of V_3O_7/GO heterostructures and V_2O_5 can be displayed by the CV curves at 0.6 mV s^{-1} is displayed in Fig. 4c and Figure S8c, respectively. The distribution of surface-controlled capacity contributions and diffusion-controlled capacity contributions at the different scan rates of V_3O_7/GO heterostructures as shown in Fig. 4d, where the surface-controlled capacity contribution enhances from 57.7 to 87.0% with the increased scan rate from 0.2 to 5 mV s^{-1}. The increased surface-controlled

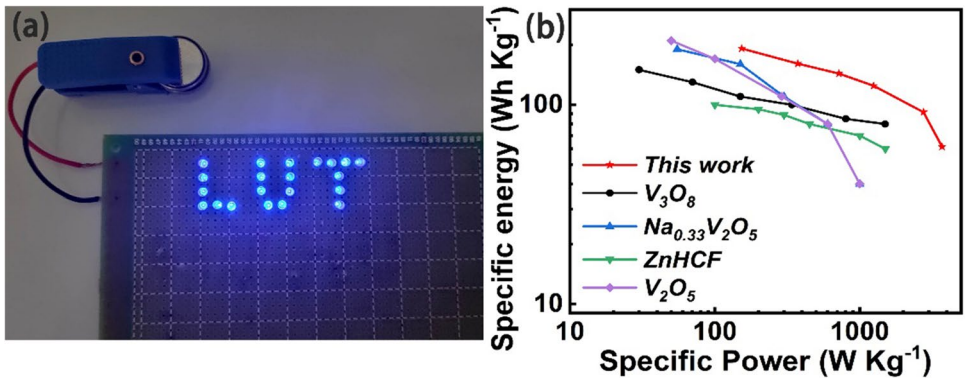

Fig. 5 **a** The Zn||V_3O_7/GO batteries were employed to light the LED bulb. **b** The Ragone plot of the Zn||V_3O_7/GO battery compared with other aqueous ZIBs

capacity contribution indicates that V_3O_7/GO possesses a rapid reaction rate, which caused by the increased specific surface area and promoted conductivity by forming heterostructures. The surface-controlled capacity contribution of V_2O_5 enhances from 39.3 to 76.9% with the same scan rate (Figure S8d). It is clear that surface-controlled capacity contribution of V_3O_7/GO heterostructures is higher than that of V_2O_5, which proved the outstanding kinetic performance of V_3O_7/GO. The reaction kinetic analysis of V_3O_7/GO heterostructures and V_2O_5 was conducted by the electrochemical impedance spectroscopy (EIS). The corresponding Nyquist plots of V_3O_7/GO heterostructures and V_2O_5 were tested from 0.01 Hz to 100 kHz. The semicircle is the high frequency area, which represents the charge transfer resistance (R_{ct}) at the electrode/electrolyte interface. The R_{ct} of V_3O_7/GO heterostructures is smaller than that of V_2O_5 in Fig. 4e, confirming that the storage reaction of Zn^{2+} in V_3O_7/GO heterostructures is easier than that in V_2O_5 because of the promoted conductivity and increased specific surface area of V_3O_7/GO heterostructures. The straight line is the low frequency area, which represents the Zn^{2+} diffusion resistance within the electrodes. The slope of the V_3O_7/GO heterostructures is much steeper than V_2O_5, indicating faster Zn^{2+} diffusion in V_3O_7/GO heterostructures/electrolyte interface than that of V_2O_5. The rate capability is significantly improved due to the rapid diffusion rate of Zn^{2+} and the result can be further confirmed by the capacity retention rate in Fig. 4f. The tight attachment of V_3O_7 and GO with enlarged surface area provides a large interface of electrolyte/electrode and rapid charge transfer for the storage of Zn^{2+}, which improves the reaction kinetic performance.

To illustrate the practicality of V_3O_7/GO heterostructures, the Zn‖V_3O_7/GO ZIBs were assembled employed Zn foil as anode and V_3O_7/GO heterostructures as cathode. The working voltage can reach 3.0 V by two batteries in series and the LED lights can be driven in Fig. 5a. The Ragone plot of ZIBs is displayed in Fig. 5b, and the Zn‖V_3O_7/GO ZIBs deliver a high energy density of 191.8 Wh kg^{-1} at the power density of 153.4 W kg^{-1} and the energy density of 61.6 Wh kg^{-1} at the power density of 3696 W kg^{-1}. The result is higher than the currently reported V_3O_8 [27], $Na_{0.33}V_2O_5$ [38], ZnHCF [39], and V_2O_5 [40], which confirms the V_3O_7/GO heterostructures electrode possesses a favorable practicability.

Conclusions

In summary, V_3O_7/GO heterostructures were successfully synthesized by a hydrothermal reaction, and the heterostructures were formed due to the V_3O_7 nanosheets were tightly attached on GO surface. The V_3O_7/GO heterostructures possess a high structural stability and large specific surface area, which displays high specific capacity and outstanding cycle stability. The specific capacity of V_3O_7/GO heterostructures is 275.6 mA h g^{-1} at the current density of 1.0 A g^{-1} and the capacity retention is 79.6% after 200 cycles. The excellent Zn^{2+} storage performance of V_3O_7/GO heterostructures can be attributed to the following advantages: (i) The enlarged specific surface area can provide abundant active sites for the storage of Zn^{2+}, (ii) V_3O_7/GO heterostructures can remain an outstanding structural stability, and (iii) the electrical conductivity is enhanced due to the addition of GO. The study paves the way for promoting the Zn^{2+} storage performance of vanadium oxide and developing stable cathode materials of ZIBs.

Supplementary Information The online version contains supplementary material available at https://doi.org/10.1007/s11581-021-04255-y.

Funding This work was supported by the National Natural Science Foundation of China (No. 52062030), the Found of the State Key Laboratory of Advance Processing and Recycling of Non-ferrous Metals, Lanzhou University of Technology (No. SKLAB02019008), and Hongliu Youth Fund of Lanzhou University of Technology.

References

1. Kundu D, Adams B, Duffort V, Linda F (2016) A high-capacity and long-life aqueous rechargeable zinc battery using a metal oxide intercalation cathode. Nat Energy 1(10):16119
2. Fang G, Zhou J, Pan A, Liang S (2018) Recent advances in aqueous zinc-ion batteries. ACS Energy Lett 3(10):2480–2501
3. Canepa P, Sai Gautam G, Hannah D, Liu M, Gallagher K, Persson K, Ceder G (2017) Odyssey of multivalent cathode materials: open questions and future challenges. Chem Rev 117(5):4287–4341
4. Liu Y, Li Q, Ma K, Yang G, Wang C (2019) Graphene oxide wrapped CuV_2O_6 nanobelts as high-capacity and long-life cathode materials of aqueous zinc-ion batteries. ACS Nano 13(10):12081–12089
5. Wang X, Li Y, Wang S, Zhou F, Das P, Sun C, Wu Z (2020) 2D amorphous V_2O_5/graphene heterostructures for high-safety aqueous Zn-ion batteries with unprecedented capacity and ultrahigh rate capability. Adv Energy Mater 10(22):2000081
6. Zhao J, Ren H, Liang QH, Yuan D, Xi S, Yan Q (2019) High-performance flexible quasi-solid-state zinc-ion batteries with layer-expanded vanadium oxide cathode and zinc/stainless steel mesh composite anode. Nano Energy 62:94–102
7. Zhou Q, Zheng Y, Wang D, Lian Y, Ban C, Zhao J, Zhang H (2020) Cathode materials in non-aqueous aluminum-ion batteries: progress and challenges. Ceram Int 46(17):26454–26465
8. Pan H, Shao Y, Yan P, Cheng Y, Han S, Liu J (2016) Reversible aqueous zinc/manganese oxide energy storage from conversion reactions. Nat Energy 1(5):16039
9. Song W-J, Lee S, Song G, Han D-Y, Jeong I, Park S (2020) Recent progress in aqueous based flexible energy storage devices. Energy Storage Mater 30:260–286
10. Tong Y, Gao A, Zhang Q, Gao T, Yue J, Gu L (2021) Cation-synergy stabilizing anion redox of Chevrel phase Mo_6S_8 in aluminum ion battery. Energy Storage Mater 37:87–93
11. Ye Z, Xie S, Cao Z, Wang L, Xu D, Zhang H, Ye M (2021) High-rate aqueous zinc-organic battery achieved by lowering HOMO/LUMO of organic cathode. Energy Storage Mater 37:378–386

12. Yang W, Du X, Zhao J, Chen Z, Li J, Cui GL (2020) Hydrated eutectic electrolytes with ligand-oriented solvation shells for long-cycling zinc-organic batteries. Joule 4(7):1557–1574
13. Xia C, Guo J, Li P, Alshareef N (2018) Highly stable aqueous zinc-ion storage using a layered calcium vanadium oxide bronze cathode. Angew Chem Int Ed Engl 57(15):3943–3948
14. Ming F, Liang H, Lei Y, Kandambeth S, Alshareef N (2018) Layered $Mg_XV_2O_5{\cdot}nH_2O$ as cathode material for high-performance aqueous zinc ion batteries. ACS Energy Lett 3(10):2602–2609
15. Ming J, Guo J, Xia C (2019) Zinc-ion batteries: materials, mechanisms, and applications. Mater Sci Eng R Rep 135:58–84
16. Dai X, Wan F, Zhang L, Zhang L, Cao HM, Niu Z (2019) Free-standing graphene/VO_2 composite films for highly stable aqueous Zn-ion batteries with superior rate performance. Energy Storage Mater 17:143–150
17. Gao J, Xie X, Liang S, Lu B, Zhou J (2021) Inorganic colloidal electrolyte for highly robust zinc-ion batteries. Nano-Micro Lett 13:69
18. Lu Q, Bishop R, Lee D, Lee S, Bluhm H, Yildiz B (2018) Electrochemically triggered metal–insulator transition between VO_2 and V_2O_5. Adv Func Mater 28:1803024
19. Chen D, Lu M, Wamg B, Cheng H, Yang H, Fang H (2021) High-mass loading $V_3O7{\cdot}H_2O$ nanoarray for Zn-ion battery: new synthesis and two-stage ion intercalationchemistry. Nano Energy 83:105835
20. Cao H, Zheng Z, Norby P, Xiao X, Mossin S (2021) Electrochemically induced phase transition in VO·HO nanobelts/reduced graphene oxide composites for aqueous zinc-ion batteries. Small 17(24):2100558
21. Wang X, Xi B, Ma X, Feng ZY, Xiong S (2020) Boosting zinc-ion storage capability by effectively suppressing vanadium dissolution based on robust layered barium vanadate. Nano Lett 20(4):2899–2906
22. Shan L, Zhou J, Zhang W, Xia C, Guo S, Liang S (2019) Highly reversible phase transition endows V_6O_{13} with enhanced performance as aqueous zinc-ion battery cathode. Energ Technol 7(6):1900022
23. Tamilselvan M, Sreekanth TVM, Yoo K, Kim J (2021) Wide interlayer spacing ammonium vanadate $(NH_4)_{0.37}V_2O_5.0.15(H_2O)$ cathode for rechargeable aqueous zinc-ion batteries. J Ind Eng Chem 93:176–185
24. Yang Y, Tang Y, Fang G, Shan L, Guo J, Liang S (2018) Li^+ intercalated $V_2O_5{\cdot}nH_2O$ with enlarged layer spacing and fast ion diffusion as an aqueous zinc-ion battery cathode. Energy Environ Sci 11(11):3157–3162
25. He P, Zhang G, Liao X, Yan M, Xu X, Mai L (2018) Sodium ion stabilized vanadium oxide nanowire cathode for high-performance zinc-ion batteries. Adv Energy Mater 8(10):1702463
26. Jiang H, Zhang Y, Xu L, Gao Z, Zheng J, Wang J (2020) Fabrication of $(NH_4)_2V_3O_8$ nanoparticles encapsulated in amorphous carbon for high capacity electrodes in aqueous zinc ion batteries. Chemical Eng J 382:122844
27. Yang G, Wu M, Wang C (2016) Ultrathin $Zn_2(OH)_3VO_3$ nanosheets: first synthesis, excellent lithium-storage properties, and investigation of electrochemical mechanism. ACS Appl Mater Interfaces 8(36):23746–23754
28. Zhu K, Wu T, Huang K (2019) $NaCa_{0.6}V_6O_{16}{\cdot}3H_2O$ as an ultrastable cathode for Zn-ion batteries: the roles of pre-inserted dual-cations and structural water in V_3O_8 layer. Adv Energy Mater 9(38):1901968
29. Shan L, Yang Y, Zhang W, Chen H, Fang G, Liang S (2019) Observation of combination displacement/intercalation reaction in aqueous zinc-ion battery. Energy Storage Mater 18:10–14
30. Jiang S, Huang C, Cao H, Wang K, Chen H (2020) Citrate-mediated synthesis of highly crystalline transition metal hexacyanoferrates and their Na ion storage properties. Appl Surf Sci 531:147336
31 Li Q, Zhang Q, Liu C, Zhou Z, Li C, Yang Y (2019) Anchoring V_2O_5 nanosheets on hierarchical titanium nitride nanowire arrays to form core-shell heterostructures as superior cathode for high-performance wearable aqueous rechargeable zinc-ion batteries. J Mater Chem A 7:12997–13006
32. Yan M, He P, Chen Y (2018) Water-lubricated intercalation in $V_2O_5.nH_2O$ for high-capacity and high-rate aqueous rechargeable zinc batteries. Adv Mater 30(1):1703725
33. Fei L, Chen Z, Fang G, Wang Z, Cai Y, Tang B, Jiang Z, Liang S (2019) V_2O_5 nanospheres with mixed vanadium valences as high electrochemically active aqueous zinc-ion battery cathode. Nano-Micro Lett 11(1):25
34. Hu T, Liu Y, Zhang Y, Meng C, Zheng J, Jie T, Meng C (2018) 3D hierarchical porous $V_3O_7{\cdot}H_2O$ nanobelts/CNT/reduced graphene oxide integrated composite with synergistic effect for supercapacitors with high capacitance and long cycling life. J Colloid Interface Sci 531:382–393
35. Zhang Y, Zhang B, Hu Y, Li J, Chueh Y (2021) Diamine molecules double lock-link structured graphene oxide sheets for high-performance sodium ions storage. Energy Storage Mater 34:45–52
36. Zhang Y, Yang Z, Zhang B, Li J, Lu C, Liu M (2020) Self-assembly of secondary-formed multilayer La/e-Ti_3C_2 as high performance supercapacitive material with excellent cycle stability and high rate capability. J Alloys Compd 835:155343
37. Hu F, Xie D, Cui F, Zhang D, Song G (2019) Synthesis and electrochemical performance of NaV_3O_8 nanobelts for Li/Na-ion batteries and aqueous zinc-ion batteries. RSC Adv 9(36):20549–20556
38. Zhang C, Park S-H, O'brien SE, Liang M, Nicolosi V (2017) Liquid exfoliation of interlayer spacing-tunable 2D vanadium oxide nanosheets: high capacity and rate handling Li-ion battery cathodes. Nano Energy 39:151–161
39. Silva M, Ardisson J, Fabris J, Nossol E (2020) Zinc hexacyanoferrate/multi-walled carbon nanotubes films for rechargeable aqueous batteries. J Braz Chem Soc 9(31):1787–1795
40. Jing P, Wei W, Luo W, Li X, Wei M, Yu D, Liu G (2020) In-situ XRD study of the structure and electrochemical performance of V_2O_5 nanosheets in aqueous zinc ion batteries. Inorg Chem Commun 117:107953